IL NUOVO CIMENTO **39 C** (2016) 310
DOI 10.1393/ncc/i2016-16310-2

Colloquia: La Thuile 2016

GW150914: Observation of gravitational waves from a binary black hole merger

F. Marion on behalf of the LIGO Scientific Collaboration and the Virgo Collaboration

Laboratoire d'Annecy-le-Vieux de Physique des Particules (LAPP), Université Savoie Mont Blanc - CNRS/IN2P3, F-74941 Annecy-le-Vieux, France

received 26 July 2016

Summary. — This article provides an overview of the first direct detection of a gravitational wave signal —GW150914— from a binary black hole merger, of the properties of the source and the implications in terms of astrophysics and fundamental physics.

1. – Introduction

A century after gravitational waves (GW) were predicted by Einstein as part of his theory of general relativity (GR), the Laser Interferometer Gravitational-wave Observatory (LIGO) detected a signal from a binary black hole merger. GW150914 was recorded by the two LIGO detectors at Hanford (H1), WA, and Linvingston (L1), LA, on September 14, 2015, at 09:50:45 UTC, with a signal-to-noise ratio (SNR) of 24 and a significance greater than 5.1σ. This discovery was reported in [1], with relevant details laid out in a number of companion papers [2-13].

2. – Detectors

On September 14, 2015, the H1 and L1 detectors were taking science quality data in the transition period between the ER8 engineering run and the O1 observing run. They were being operated in an Advanced LIGO configuration, following the upgrade that took place after the S6 science run of the initial LIGO detectors [2]. The Virgo detector was being upgraded, and GEO 600 was not in observational mode. After the early detection of GW150914, H1 and L1 were kept in the same configuration until October 20, to provide a homogeneous set of coincident science data (16 days, accounting for the detectors duty cycle) to assess the significance of the event.

The sensitivity of the H1 and L1 detectors during that reference period is shown in fig. 1. In the best frequency band—100–300 Hz— they were 3 to 4 times more sensitive

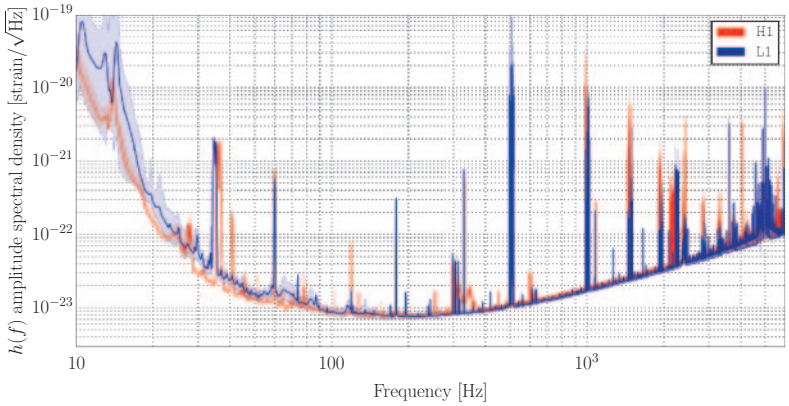

Fig. 1. – Measured strain sensitivity of the Advanced LIGO detectors (H1, red, and L1, blue) during the period from Sept 12 to Oct 20, 2015. The solid traces represent the median sensitivity and the shaded regions indicate the 5th and 95th percentile over the analysis period.

than the initial detectors, and much more at low frequencies. At the time of GW150914, H1 had been in observation mode for about 30 minutes, and L1 for more than an hour.

The detectors physical environment is monitored with an array of sensors: seismometers, accelerometers, microphones, magnetometers, radio receivers, weather sensors, AC-power line monitors, cosmic ray detector, representing about 10^5 channels for each detector. They are used to characterize couplings to the GW channel and to identify and veto transient disturbances. Special attention is paid to possible correlated sources of noise such as global electromagnetic noise. An environmental origin for GW150914 was ruled out as the excess power in any auxiliary channel was too small by a factor of at least 17 to account for the amplitude of GW150914, let alone match the signal morphology [3].

3. – Searches

Dedicated searches for compact binary coalescence (CBC) signals [5] rely on accurate models of the expected waveforms to analyze the data with matched filtering. Those searches target signals from binary neutron star, binary black hole or neutron star–black-hole systems. The instrinsic parameters of the source drive the system dynamics and waveform evolution, therefore the searches employ a discrete set of about 250,000 templates to scan the four-dimensional space of masses and spin projections to the orbital momentum, as shown in fig. 2. Triggers are extracted as maxima in the SNR time series for each template and each detector. They are subjected to a test checking consistency of the signal with the expected waveform and to data quality vetoes excluding times with known perturbations in the instruments or their environments. Coincidences are then identified as surviving triggers in the two detectors matching in time and parameters.

Triggers are ranked according to the value of the combined reweighted SNR: $\hat{\rho}_c = \sqrt{\hat{\rho}^2_{H1} + \hat{\rho}^2_{L1}}$, with $\hat{\rho} = \rho/[(1 + (\chi^2_r)^3)/2]^{1/6}$ and χ^2_r the outcome of the consistency test. GW150914 was the loudest event in the CBC search, with $\hat{\rho}_c = 23.6$, and the single detector triggers forming GW150914 also had the largest $\hat{\rho}$ in H1 and L1. The signal significance is quantitatively assessed based on its false alarm rate (FAR), measured from the background estimated on the data themselves: The analysis is repeated $\sim 10^7$ times on detector streams time-shifted by multiples of 0.1 s, whereby accumulating a

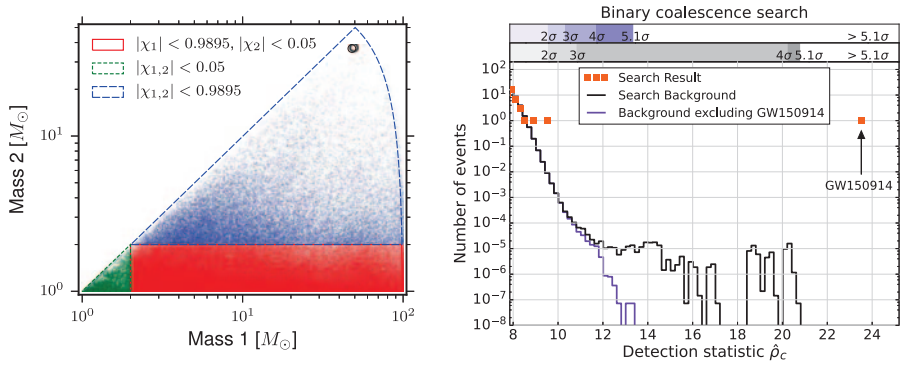

Fig. 2. – Left: Four-dimensional search parameter space covered by the template bank used in the CBC searches. Right: Search results from the CBC search. The histograms show the number of candidate events (orange markers) and the mean number of background events (black lines) as a function of the search detection statistic. The scales on the top give the significance of an event in Gaussian standard deviations based on the corresponding noise background.

background time of 608 000 years. As shown in fig. 2, GW140914 is louder than all background triggers, therefore bounding its false alarm probability after accounting for trial factors to be $< 2 \times 10^{-7}$, corresponding to $> 5.1\sigma$.

Data are also analyzed with a generic transient search [6], which operates without a specific waveform model. It identifies coincident excess power in time-frequency representations of the GW data, with durations below a few seconds and frequencies below 1 kHz. It reconstructs signal waveforms that are consistent with the common signal in the two instruments using a multi-detector maximum likelihood method. Signals are

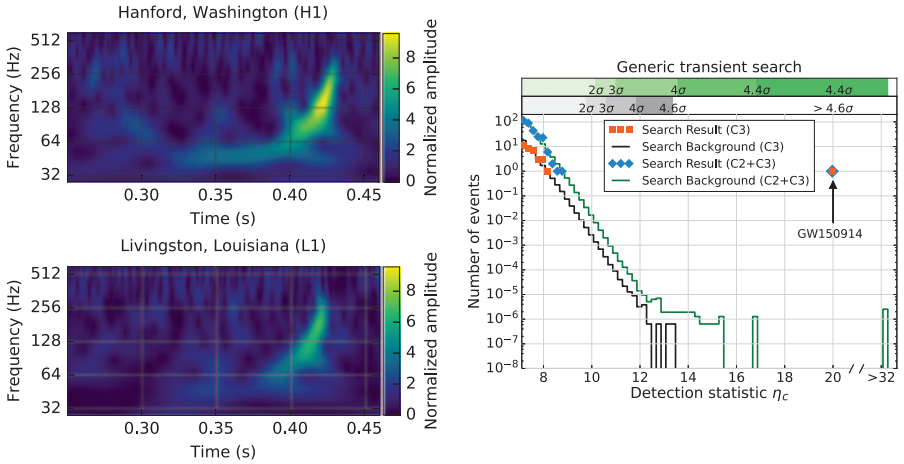

Fig. 3. – Left: Time-frequency representation of the strain data, showing GW150914's frequency increasing over time. Right: Search results from the generic transient search. The histograms show the number of candidate events (orange markers) and the mean number of background events (black lines) as a function of the search detection statistic. The scales on the top give the significance of an event in Gaussian standard deviations based on the corresponding noise background.

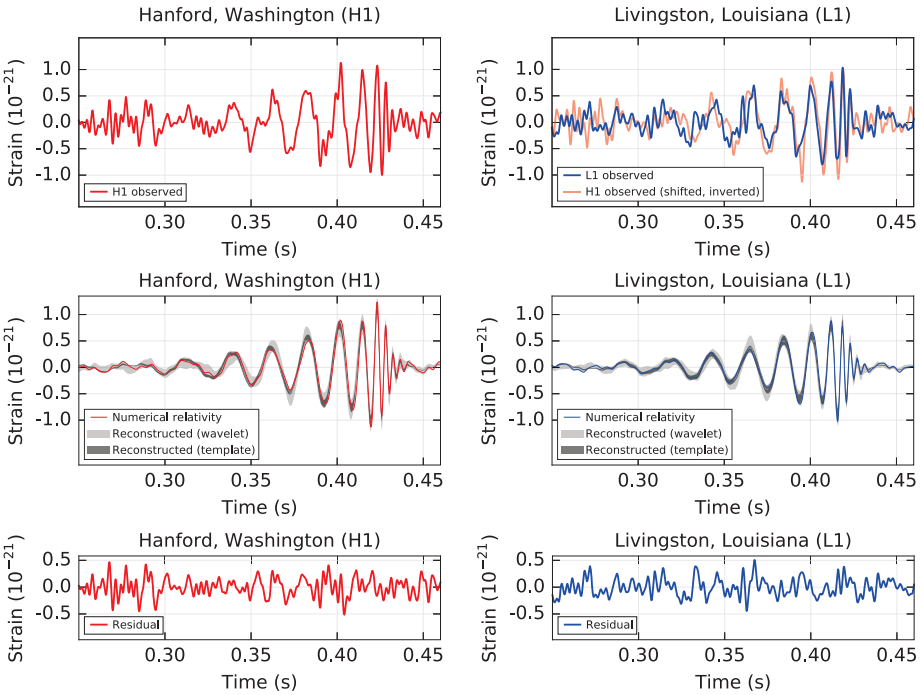

Fig. 4. – GW150914 signal observed by the LIGO H1 (left) and L1 (right) detectors, filtered with a 35–350 Hz bandpass filter. Top: Strain data. Middle: GW strain projected onto each detector, showing a numerical relativity waveform for a system with parameters consistent with those recovered from GW150914 (solid lines) and 90% credible regions for two independent waveform reconstructions (shaded areas). Bottom: Residuals after subtracting the filtered numerical relativity waveform from the filtered detector time series.

ranked according to the detection statistic $\eta_c = \sqrt{2E_c/(1+E_n/E_c)}$, where E_c is the dimensionless coherent signal energy obtained by cross-correlating the two reconstructed waveforms, and E_n is the dimensionless residual noise energy after the reconstructed signal is subtracted from the data. Signals are then divided into three search classes based on their time-frequency morphology. GW150914 was found in the class of events with frequency increasing with time, as is expected for a CBC signal and as can be seen on fig. 3. GW150914 was the loudest event in that search class, with $\eta_c = 20.0$. Its significance in this search is also measured from time slides, with a false alarm probability bound to be less than $< 2 \times 10^{-6}$ equivalent to $> 4.6\,\sigma$, see fig. 3.

Figure 4 shows the strain time series measured in the H1 and L1 detectors, and compares them to various waveform reconstructions. The waveform reconstructed from the coherent signal in both detectors agrees with the best-fit CBC waveform, with a numerical relativity waveform computed for a system with parameters consistent with those recovered from GW150914, and with the data.

4. – Source properties and implications

Eight instrinsic parameters are needed to describe the source (masses and spin vectors) and, assuming circular orbits, seven extrinsic parameters: three for the location

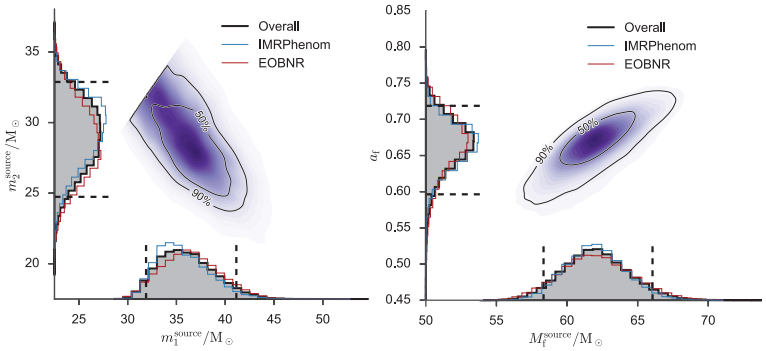

Fig. 5. – Posterior PDFs inferred from parameter estimation using two different waveform models. Left: Source-frame component masses $m_1^{\rm source}$ and $m_2^{\rm source}$, where $m_2^{\rm source} < m_1^{\rm source}$. Right: Source-frame mass and spin of the remnant BH produced by the coalescence of the binary.

(luminosity distance, right ascension, declination), two for the orientation (inclination and polarization) and two for the time and phase of coalescence. Those parameters are estimated from a coherent analysis across the detector network, in a Bayesian framework [7]: Stochastic sampling methods are used to explore the full multidimensional parameter space, computing the likelihood of the data according to the match between the data and the predicted waveform given a set of parameters. Parameter estimation therefore relies on accurate waveform models being available, which has made crucial progress over the past decade. There are now models that combine perturbative theory and numrical relativity and accurately describe all the phases of a BBH coalescence: inspiral, merger, and ringdown.

The intrinsic parameters of the binary drive the system dynamics and are therefore encoded in the GW signal. The inspiral phase is driven at leading order by a combination of the individual masses called the chirp mass. The mass ratio and spin components parallel to the orbital angular momentum enter at next to leading order, and other spin degrees of freedom ar higher orders. In addition, if spins have components in the orbital plane, this leads the latter to precess, causing amplitude and phase modulation of the observed GW signal. The merger and ringdown phases are primarily governed by the mass and spin of the final black hole, which are fully determined by the masses and spins of the binary in GR.

Figure 5 shows the posterior probability density functions (PDF) for the source-frame component masses, which are measured to be $m_1^{\rm source} = 36^{+5}_{-4}\,{\rm M}_\odot$ and $m_2^{\rm source} = 29^{+4}_{-4}\,{\rm M}_\odot$, and for the source-frame mass and spin of the remnant BH produced by the coalescence of the binary, which are measured to be $M_f^{\rm source} = 62^{+4}_{-4}\,{\rm M}_\odot$ and $a_f = 0.67^{+0.05}_{-0.07}$. We estimate the system radiated in GW a total energy of $3.0^{+0.5}_{-0.4}\,{\rm M}_\odot c^2$ and reached a peak luminosity of $3.5^{+0.5}_{-0.4} \times 10^{56}\,{\rm erg/s}$, equivalent to $200^{+30}_{-20}\,{\rm M}_\odot c^2/{\rm s}$.

The detection and properties of GW150914 demonstrate that relatively heavy stellar-mass black holes ($> 25\,{\rm M}_\odot$) exist in nature, which implies the progenitor was formed in a low metallicity environment, to allow for weak massive-star winds. Also demonstrated is the fact that binary black holes can form, although GW150914 does not allow to identify the formation path, from an isolated binary or through dynamical capture in a dense star cluster [8]. GW150914 also implies that binary black holes can merge within the age

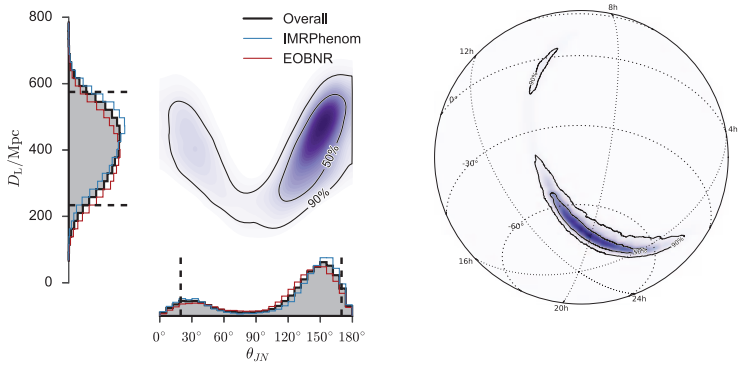

Fig. 6. – Left: Posterior PDFs inferred from parameter estimation using two different waveform models, for the source luminosity distance and the binary inclination. Right: Sky location of GW150914 showing contours of the 50% and 90% credible regions over a colour-coded PDF.

of the Universe, at a rate inferred to be in the range 2–400 $\mathrm{Gpc}^{-3}\,\mathrm{yr}^{-1}$, consistent with the higher end of rate predictions [9].

The estimation of extrinsic parameters is based both on measurements and statistical guesses. The amplitude of the observed signal depends on the system intrinsic properties and its distance, as well as some geometrical factors. There is for instance a degeneracy between the distance and the inclination of the system with respect to the line of sight (see fig. 6), with distant sources with favorable orientations being more likely. The source luminosity distance is estimated to be 410^{+160}_{-180} Mpc, corresponding to a redshift $z = 0.09^{+0.03}_{-0.04}$. The sky location of the source is inferred primarily from the time delay of $6.9^{+0.5}_{-0.4}$ ms between the L1 and H1 detectors, as well as amplitude and phase consistency constraints, with sky locations corresponding to good detector response being preferred. The localization currently has limited accuracy, with a two detector network, and forms part of an annulus whose area is about 600 deg^2.

5. – Follow-up searches

Preliminary estimates of the time, significance, and sky location of GW150914 were shared with 63 teams of astronomy partners covering radio, optical, near-infrared, X-ray, and gamma-ray wavelengths with ground- and space-based facilities. Follow-up observations were reported by 25 teams in the days and weeks that followed [11], covering a fair fraction of the preliminary sky map, as can be seen in fig. 7. As GW150914 turned out to be a binary black hole merger, there is little expectation of a detectable electromagnetic signature. Nevertheless, this first broadband campaign to search for a counterpart of a GW source represents a milestone and highlights the broad capabilities of the transient astronomy community.

Another follow-up of GW150914 was performed, searching for coincident high-energy neutrinos in the data recorded by the IceCube and ANTARES detectors [12], as could be expected in the unlikely scenario where a black hole plus accretion disk system is formed. No neutrino candidate was identified in both temporal and spatial coincidence: No neutrino candidate was found in the ANTARES data within ± 500 s of GW150914; three were found in the IceCube data—none of which were directionally coincident with

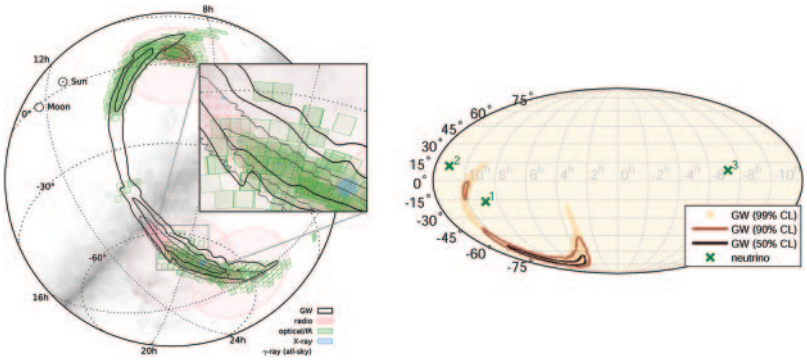

Fig. 7. – Left: Footprints of electromagnetic observations in comparison with the 50% and 90% credible levels of the initially distributed GW localization maps. Right: GW150914 sky map with the reconstructed directions of high-energy neutrino candidates detected by IceCube (crosses) during a $\pm 500\,\mathrm{s}$ time window around GW150914.

GW150914 as can be seen in fig. 7— which is consistent with the expected atmospheric background. This allows to derive a direction dependent neutrino fluence upper limit as well as an upper limit on the total energy emitted in neutrinos by the source.

6. – Consistency with general relativity

GW150914 allows to test GR in the strong field, non linear, high velocity regime ($v/c \sim 0.5$). Although it is a single event, its relatively large SNR allows to perform some coarse consistency tests with the predictions of GR [13]. It was checked that the residuals after subtraction of the best-fit waveform are consistent with instrumental noise, and that early and late parts of the observed waveforms are consistent with each other in the context of GR. By using waveform models that allow for parameterized GR violations during the inspiral and merger phases, quantitative tests were performed on the GW phase in the dynamical regime and the first empirical bounds were placed on several high-order post-Newtonian coefficients (see fig. 8). Furthermore, assuming a modified dispersion relation for gravitational waves, GW150914 constrains the Compton wavelength of the graviton to be $\lambda_g > 10^{13}\,\mathrm{km}$, which could be interpreted as a bound on the graviton mass $m_g < 1.2 \times 10^{-22}\,\mathrm{ev}/c^2$.

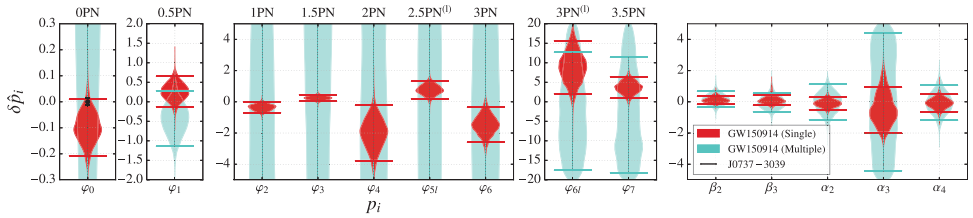

Fig. 8. – Posterior PDFs of parameters caracterizing deviations from GR in the GW150914 signal. The φ parameters are related to the early inspiral phase, while the α and β parameters pertain to the late inspiral, merger and rindown phases.

7. – Outlook

Efforts are underway to enhance significantly the global gravitational wave detector network, both in terms of sensitivity and number of detectors, with Advanced Virgo expected to join Advanced LIGO soon. The future observing runs will lead to detecting further signals, with improved position reconstruction and parameter estimation of the sources, thus yielding a wealth of astrophysics and fundamental physics insights.

REFERENCES

[1] LIGO Scientific Collaboration, Virgo Collaboration (Abbott B. P. *et al.*), *Phys. Rev. Lett.*, **116** (2016) 061102.
[2] LIGO Scientific Collaboration, Virgo Collaboration (Abbott B. P. *et al.*), *Phys. Rev. Lett.*, **116** (2016) 131103.
[3] LIGO Scientific Collaboration, Virgo Collaboration (Abbott B. P. *et al.*), *Class. Quantum Grav.*, **33** (2016) 134001, arXiv:1602.03844 [gr-qc].
[4] LIGO Scientific Collaboration (Abbott B. P. *et al.*), (2016) arXiv:1602.03845 [gr-qc].
[5] LIGO Scientific Collaboration, Virgo Collaboration (Abbott B. P. *et al.*), *Phys. Rev. D*, **93** (2016) 122003, arXiv:1602.03839 [gr-qc].
[6] LIGO Scientific Collaboration, Virgo Collaboration (Abbott B. P. *et al.*), *Phys. Rev. D*, **93** (2016) 122004, arXiv:1602.03843 [gr-qc].
[7] LIGO Scientific Collaboration, Virgo Collaboration (Abbott B. P. *et al.*), *Phys. Rev. Lett.*, **116** (2016) 241102, arXiv:1602.03840 [gr-qc].
[8] LIGO Scientific Collaboration, Virgo Collaboration (Abbott B. P. *et al.*), *Astrophys. J. Lett.*, **818** (2016) L22.
[9] LIGO Scientific Collaboration, Virgo Collaboration (Abbott B. P. *et al.*), (2016), arXiv:1602.03842 [astro-ph.HE].
[10] LIGO Scientific Collaboration, Virgo Collaboration (Abbott B. P. *et al.*), *Phys. Rev. Lett.*, **116** (2016) 131102.
[11] Abbott B. P. *et al.*, *Astrophys. J.*, **826** (2016) L13, arXiv:1602.08492 [astro-ph.HE].
[12] ANTARES Collaboration, IceCube Collaboration, LIGO Scientic Collaboration, and Virgo Collaboration (Adrin-Martnez S. *et al.*), *Phys. Rev. D*, **93** (2016) 122010, arXiv:1602.05411 [astro-ph.HE].
[13] LIGO Scientific Collaboration, Virgo Collaboration (Abbott B. P. *et al.*), *Phys. Rev. Lett.*, **116** (2016) 221101, arXiv:1602.03841 [gr-qc].